Regular Article – Theoretical Physics

Timelike Compton scattering off the proton and generalized parton distributions

M. Boër[1], M. Guidal[1,a], and M. Vanderhaeghen[2]

[1] Institut de Physique Nucléaire d'Orsay, CNRS-IN2P3, Université Paris-Sud, F-91406 Orsay, France
[2] Institut für Kernphysik and PRISMA Cluster of Excellence, Johannes Gutenberg Universität, D-55099 Mainz, Germany

Abstract. We study the exclusive photoproduction of a lepton pair off the proton with the aim of studying the proton quark structure via the Generalized Parton Distributions (GPD) formalism. After deriving the amplitudes of the processes contributing to the $\gamma P \to P' e^+ e^-$, the timelike Compton scattering and the Bethe-Heitler process, we calculate all unpolarized, single- and double- spin beam-target observables in the valence region in terms of GPDs.

1 Introduction

The scattering of light on matter, which can generically be called Compton scattering, is a powerful tool to investigate its inner structure. Nowadays, understanding the structure of hadrons in terms of quark and gluon (partons) degrees of freedom, *i.e.* the basic constituents of matter known to this day, is the subject of an intense research effort. Only these past fifteen years or so, thanks to the emergence of high-intensity, high-energy (multi-GeV) and high duty-cycle lepton accelerators, Compton scattering at the partonic level starts to be investigated experimentally in an efficient way.

A particular case of Compton scattering at the partonic level is the Deeply Virtual Compton Scattering (DVCS) process on the proton P, *i.e.* $\gamma^* P \to \gamma P'$ where the initial virtual photon γ^* is radiated from an incoming lepton beam (see fig. 1, top). It is of particular interest as the amplitude of the process allows to access some essential operators of Quantum Chromo-Dynamics (QCD, the fundamental theory governing the interactions of quarks and gluons). Indeed, at sufficiently large virtuality of the initial photon ($Q^2 = (k - k')^2$), the DVCS amplitude can be factorized into an elementary "hard" (perturbative) scattering process $\gamma^* q \to \gamma q$ (where q is a quark of the proton), exactly calculable from Quantum Electro-Dynamics (QED) as well as perturbative QCD, and a "soft" (nonperturbative) QCD bilocal matrix elements. The Fourier transforms into momentum space of these QCD matrix elements are the so-called Generalized Parton Distributions (GPDs). In DVCS on the nucleon, at QCD leading-twist order there are four quark helicity conserving GPDs

($H, E, \tilde{H}$ and $\tilde{E}$) which can be accessed and which correspond to the four independent helicity-spin transitions between the initial quark-proton system and the final one. The GPDs contain a wealth of information on the partonic structure of the proton: the longitudinal momentum and transverse space distributions of the quarks and gluons, the correlation between these momentum and space distributions, sensitivity to the quark-antiquark content in the proton, the quark orbital momentum contribution to the proton spin, etc. We refer the reader to the reviews [1–4] on GPDs for the details of the formalism and of their properties.

DVCS is currently widely investigated, experimentally as well as theoretically. Reference [4] compiles all existing data in the valence region and presents some first informations on the partonic structure of the proton that can be extracted, within some approximations, from the first DVCS data through the GPD formalism. One example of a pioneering result is the first quantitative evaluation of the increase of the transverse size of the proton as smaller longitudinal momentum fractions of partons are probed.

However, the GPD information is difficult to extract: DVCS cross sections are small (of the order of pb), there is the competing Bethe-Heitler (BH) process which leads to the same final state $eP\gamma$ but where the final photon is emitted from the incoming or scattered lepton and which is therefore not related to GPDs but nevertheless interferes. Furthermore, there is the need of measuring a series of spin (beam and/or target) observables to constrain the different GPDs, etc. It would therefore be useful to investigate if supplementary and/or complementary constraints on GPDs could be obtained from processes other than DVCS. In this spirit, we investigate in this arti-

a e-mail: guidal@ipno.in2p3.fr
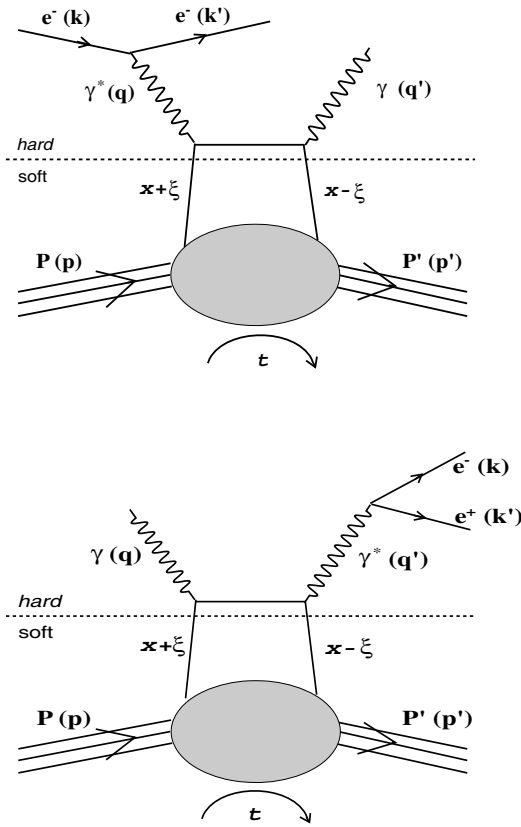
Fig. 1. Top: QCD leading-twist DVCS diagram. Bottom: QCD leading-twist TCS diagram (the crossed diagrams of both processes are not shown). The dashed line illustrates the factorization between the quark-level hard process exactly calculable in QED and the complex non-perturbative QCD nucleon structure parametrized by the GPDs.

cle the related process of Timelike Compton Scattering (TCS) which corresponds to the exclusive photoproduction of a lepton pair on the proton: $\gamma P \to P' \gamma^* \hookrightarrow e^+ e^-$ and which is displayed in fig. 1, bottom. Like for DVCS, at sufficiently large virtuality of the final virtual photon $(Q'^2 = (k + k')^2)$, it is predicted that the process factorizes and is sensitive to GPDs, the same ones accessed in DVCS.

The TCS process was originally investigated in terms of GPDs about ten years ago in ref. [5]. In this pioneering work, analytical formulas in terms of GPDs were derived for the unpolarized and the circularly polarized beam cross sections of the process $\gamma P \to P' e^+ e^-$, *i.e.* on a proton target. Very recently, a second article continued the investigation by studying the linearly polarized beam cross section [6].

However, in order to obtain simple analytical expressions, a few approximations were used in the calculation of the TCS amplitude (for instance mass correction terms of the order of m^2/Q'^2 where m is the mass of the proton were neglected). In the present work, we waive some of these approximations and present calculations of different observables. In addition, besides unpolarized cross

sections, we study all single- and double-spin beam-target observables. We focus in this article on a proton target.

This article is organized as follows: in the next section, we present the general theoretical formalism of the TCS process, in particular the expression of the QCD leading-twist amplitude in terms of GPDs, and of the accompanying BH process. We discuss some experimental considerations in the third section. In the fourth section, we present our numerical results for the unpolarized cross section of the $\gamma P \to P' e^+ e^-$ process and we compare them to the previous work of ref. [5]. In the fifth section, we present our results for single-spin observables (beam and target) and we compare our work for the beam polarization observables to the results of ref. [5]. In the sixth section, we present our results for the double-spin beam-target observables. For each case, we will show the dependence of the observables on different GPDs and its sensitivity on different kinematics. In the seventh section we show the impact of next-to-leading-twist corrections on the cross sections and on the asymmetries. We will conclude in the eighth section.

2 Formalism

We are studying the process:

$$\gamma(q)\, P(p) \to P'(p')\, e^-(k)\, e^+(k') \tag{1}$$

in a GPD framework, *i.e.* when the final photon's virtuality $Q'^2 = (k + k')^2$ is sufficiently large and the proton momentum transfer $t = (p - p')^2$ is sufficiently small so that the factorization illustrated in fig. 1, bottom can be applied. From DVCS, Deep Inelastic Scattering (DIS) and Drell-Yan analysis and experiments, it is believed that $Q'^2 > 2\,\text{GeV}^2$ and $-t < 1\,\text{GeV}^2$ should define such a reasonable phase space. Regarding Q'^2, one should also avoid regions where one can have the production of vector mesons, decaying into $e^+ e^-$ pairs (for instance, the broad $\rho'(1700)$). Additionally, one should consider the squared center-of-mass energy of the incoming photon and target proton $s = (q + p)^2 \gtrsim 4\,\text{GeV}^2$, in order to minimize possible contributions from the Dalitz decay of proton resonances. In the present work, we will consider $Q'2$ values typically around $7\,\text{GeV}^2$, and momentum transfers $-t$ typically less than $0.7\,\text{GeV}^2$. This results in ratios $\frac{-t}{Q'^2} < 10\%$, which kinematically suppresses possible higher twist terms by a factor around 10.

2.1 Kinematics

We will use the notation of Ji [7,8] for GPDs, *i.e.* GPDs depend on the three variables, x, ξ and t, where the quark longitudinal momentum fractions x and ξ are defined w.r.t. the average proton momentum P and proton momentum transfer Δ, respectively. We therefore define

$$P = \frac{1}{2}(p + p'), \tag{2}$$

$$\Delta = (p' - p) = (q - q'), \tag{3}$$

and we also introduce the average photon momentum

$$\bar{q} = \frac{1}{2}(q + q'). \qquad (4)$$

GPDs are matrix elements of QCD operators which are defined at equal light-cone time. It is therefore convenient to use a frame where the $\bar{q}$ and P momenta are collinear along the z-axis and in opposite directions. We define the lightlike vectors along the positive- and negative-z directions as

$$\tilde{p}^\mu = P^+/\sqrt{2}(1,0,0,1), \qquad (5)$$
$$n^\mu = 1/P^+ \cdot 1/\sqrt{2}(1,0,0,-1), \qquad (6)$$

and we define the light-cone components $a^\pm$ by $a^\pm \equiv (a^0 \pm a^3)/\sqrt{2}$. We have $\tilde{p}^2 = n^2 = 0$ and $\tilde{p} \cdot n = 1$. In this light-cone frame, introducing the $+$ components of the Δ and $\bar{q}$ four-vectors, $\tilde{\xi}$ and $\tilde{\xi}'$, respectively, the various four-vectors involved can be decomposed as

$$P^\mu = \tilde{p}^\mu + \frac{\bar{m}^2}{2} n^\mu, \qquad (7)$$

$$\bar{q}^\mu = -\tilde{\xi}' \tilde{p}^\mu - \frac{\bar{q}^2}{2\tilde{\xi}'} n^\mu, \qquad (8)$$

$$\Delta^\mu = -2\tilde{\xi}\tilde{p}^\mu + \tilde{\xi}\bar{m}^2 n^\mu + \Delta_\perp^\mu, \qquad (9)$$

with $\bar{m}^2 = m^2 - \frac{\Delta^2}{4}$ and m is the proton mass. We relate the final photon virtuality to the average photon momentum,

$$\bar{q}^2 = Q'^2/2 - \Delta^2/4. \qquad (10)$$

We have to relate the light-cone momentum fractions $\tilde{\xi}$ and $\tilde{\xi}'$ to the kinematical variables which are experimentally accessible. To do so, we introduce the variables ξ and ξ':

$$\xi' = -\frac{\bar{q}^2}{2P \cdot \bar{q}} = \frac{-Q'^2 + \Delta^2/2}{2(s - m^2) + \Delta^2 - Q'^2}, \qquad (11)$$

$$\xi = -\frac{\Delta \cdot \bar{q}}{2P \cdot \bar{q}} = \frac{Q'^2}{2(s - m^2) + \Delta^2 - Q'^2}. \qquad (12)$$

The light-cone momentum fractions $\tilde{\xi}$ and $\tilde{\xi}'$ are related to the kinematical variables ξ and ξ' by

$$\tilde{\xi} = \xi \cdot \frac{1 + \tilde{\xi}'^2 \bar{m}^2/\bar{q}^2}{1 - \tilde{\xi}'^2 \bar{m}^2/\bar{q}^2}, \qquad (13)$$

$$\tilde{\xi}' = \xi' \cdot \frac{2}{1 + \sqrt{1 - 4\xi'^2 \bar{m}^2/\bar{q}^2}}. \qquad (14)$$

In the asymptotic limit, where mass and Δ terms are neglected relatively to Q'^2, we have

$$\tilde{\xi} = \xi = -\tilde{\xi}' = -\xi' = \frac{Q'^2}{2s - Q'^2}. \qquad (15)$$

2.2 Timelike Compton amplitude

The two diagrams of fig. 2 have to be calculated. The leading-order amplitude reads:

$$T_H^{\text{TCS}} \propto \frac{1}{(k + \bar{q})^2 + i\epsilon} \gamma^\nu (\slashed{k} + \slashed{\bar{q}}) \gamma^\mu$$
$$+ \frac{1}{(k - \bar{q})^2 + i\epsilon} \gamma^\mu (\slashed{k} - \slashed{\bar{q}}) \gamma^\nu$$
$$\propto \frac{1}{2}\bigg[\slashed{n} (\tilde{p}^\mu n^\nu + \tilde{p}^\nu n^\mu - g^{\mu\nu})$$
$$\cdot \left(\frac{1}{x - \tilde{\xi}' + i\epsilon} + \frac{1}{x + \tilde{\xi}' - i\epsilon} \right)$$
$$- \slashed{n}\gamma_5\, i\epsilon^{\mu\nu\kappa\lambda} n_\lambda\, \tilde{p}_\kappa \left(\frac{1}{x - \tilde{\xi}' + i\epsilon} - \frac{1}{x + \tilde{\xi}' - i\epsilon} \right) \bigg]. \qquad (16)$$

The full TCS amplitude, corresponding to the diagram of fig. 1, bottom (plus the associated crossed diagram) reads then

$$T^{\text{TCS}} = -\frac{e^3}{q'^2}\, \bar{u}(k)\, \gamma^\nu\, v(k')\, \epsilon^\mu(q)\, H_{\mu\nu}^{\text{TCS}}, \qquad (17)$$

with, in the Bjorken limit where $\xi = -\tilde{\xi}'$,

$$H_{\mu\nu}^{\text{TCS}} =$$
$$\frac{1}{2} (-g_{\mu\nu})_\perp \int_{-1}^1 dx \left(\frac{1}{x - \xi - i\epsilon} + \frac{1}{x + \xi + i\epsilon} \right)$$
$$\cdot \left(H(x,\xi,t)\bar{u}(p')\slashed{n}u(p) + E(x,\xi,t)\bar{u}(p')i\sigma^{\alpha\beta}n_\alpha \frac{\Delta_\beta}{2m} u(p) \right)$$
$$- \frac{i}{2}(\epsilon_{\nu\mu})_\perp \int_{-1}^1 dx \left(\frac{1}{x - \xi - i\epsilon} - \frac{1}{x + \xi + i\epsilon} \right)$$
$$\cdot \left(\tilde{H}(x,\xi,t)\bar{u}(p')\slashed{n}\gamma_5\, u(p) + \tilde{E}(x,\xi,t)\bar{u}(p')\gamma_5 \frac{\Delta \cdot n}{2m}u(p) \right), \qquad (18)$$

where we used the metric:

$$(-g_{\mu\nu})_\perp = -g_{\mu\nu} + \tilde{p}_\mu n_\nu + \tilde{p}_\nu n_\mu,$$
$$(\epsilon_{\nu\mu})_\perp = \epsilon_{\nu\mu\alpha\beta}\, n^\alpha \tilde{p}^\beta. \qquad (19)$$

The GPDs entering eq. (18) are proton GPDs, *i.e.* they read, in terms of quark flavors:

$$H_{\text{TCS}}(x,\xi,t) = \frac{4}{9}H^{u/p} + \frac{1}{9}H^{d/p} + \frac{1}{9}H^{s/p}. \qquad (20)$$

In this work, we will take the GPD parametrizations from the VGG model [1,9–11], which are summarized in ref. [4] and based on the Radyushkin double-distribution ansatz for the (x,ξ)-dependence [12–14] and on a Reggeized ansatz for the t-distribution [1, 11]. At a couple of instances, in order to estimate the model-dependence of our calculations, we will use the factorized ansatz for the t-dependence of the H GPD [9]. Also, we will occasionally study the sensitivity of observables to the so-called D-term [15], which is included in the VGG model and whose parametrization can be found as well in refs. [1,9–11].
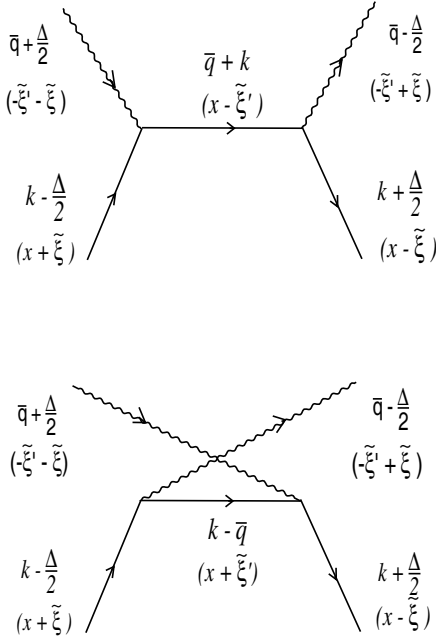
Fig. 2. Leading-order diagrams for the process $\gamma q \to \gamma q$. We indicate between parenthesis the $+$ components of the four-vectors.

2.3 Gauge invariance

The leading-twist approximation to the TCS amplitude of eq. (17) is not exactly gauge invariant. To restore gauge invariance, twist-3 corrections of order $\Delta_\perp/Q$ are needed. As a first step in adressing this issue and estimating its effect, we propose to add a correction term to the twist-2 vector part tensor as follows:

$$H^{\mu\nu} = H_{LO}^{\mu\nu} - \frac{P^\mu}{2P \cdot \bar{q}} \cdot (\Delta_\perp)_\kappa \cdot H_{LO}^{\kappa\nu}$$
$$+ \frac{P^\nu}{2P \cdot \bar{q}} \cdot (\Delta_\perp)_\lambda \cdot H_{LO}^{\mu\lambda}$$
$$- \frac{P^\mu P^\nu}{4(P \cdot \bar{q})^2} \cdot (\Delta_\perp)_\kappa \cdot (\Delta_\perp)_\lambda \cdot H_{LO}^{\kappa\lambda}, \quad (21)$$

where $H_{LO}^{\mu\nu}$ stands for the tensor of eq. (18). This is a generalization of the prescription proposed in refs. [10,16] for DVCS (we also refer the reader to refs. [17–19] for further discussions on the issue of gauge invariance in the DVCS amplitude). One can readily check that $H^{\mu\nu}$ respects gauge invariance both w.r.t. initial and final photons, *i.e.* $q_\mu H^{\mu\nu} = 0$, and $q'_\nu H^{\mu\nu} = 0$. The impact of adding this correction to the observables is shown at the end of this paper, in sect. 7.

2.4 The Bethe-Heitler amplitude

The TCS process is accompanied by the BH process, involving the two diagrams which are presented in fig. 3.
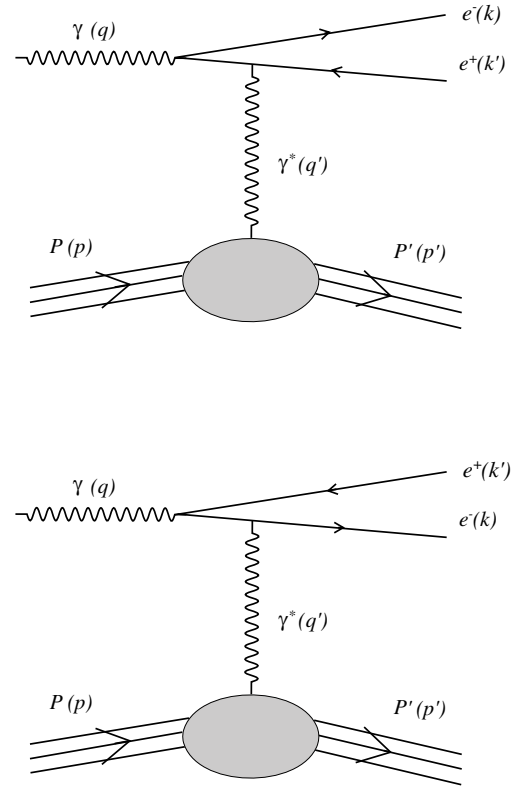
Fig. 3. The Bethe-Heitler diagrams.

Their amplitude reads

$$T^{\text{BH}} = -\frac{e^3}{\Delta^2} \bar{u}(p') \, \Gamma^\nu \, u(p) \, \epsilon^\mu(q)$$
$$\times \bar{u}(k) \left(\gamma_\mu \frac{\not{k} - \not{q}}{(k-q)^2} \gamma_\nu + \gamma_\nu \frac{\not{q} - \not{k}'}{(q-k')^2} \gamma_\mu \right) v(k'), \quad (22)$$

with the virtual photon-proton electromagnetic vertex matrix

$$\Gamma^\nu = \gamma^\nu \, F_1(t) + \frac{i\sigma^{\nu\rho}\Delta_\rho}{2\,m} \, F_2(t). \quad (23)$$

The BH amplitude depends on the proton Dirac and Pauli form factors $F_1(t)$ and $F_2(t)$. In this work, we take the parametrizations issued from refs. [20,21]. We noticed that other form factor parametrizations (for instance ref. [22]) can change the BH cross sections up to 5%. The effect on the asymmetries is however negligible.

2.5 Cross section

At fixed beam energy E_γ or longitudinal momentum transfer ξ, there are four independent kinematical variables for the process $\gamma(q)P(p) \to P'(p')e^-(k)e^+(k')$. A natural choice is to be taken: Q'^2 and $t = \Delta^2$ that we already defined, and the two angles θ and ϕ of the electron in the γ^* center of mass (with the z'-axis along the direction of the γ^* in the γ^*-P' center of mass). We illustrate
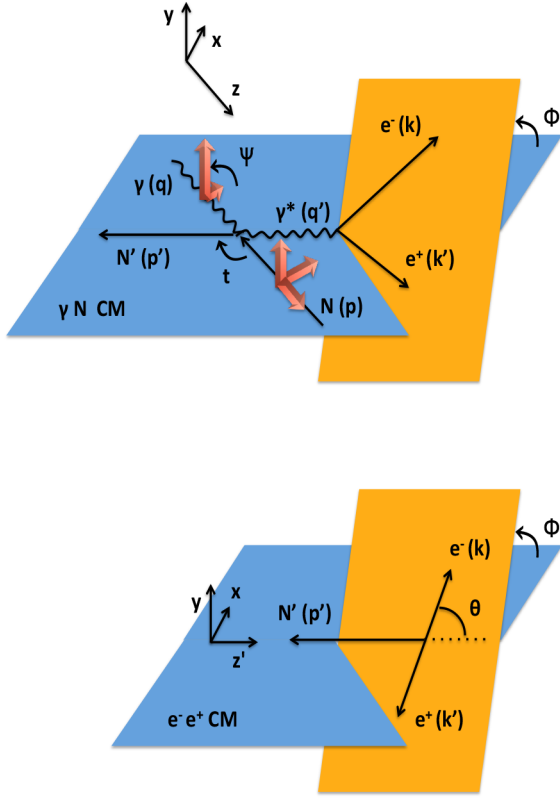
Fig. 4. Top panel: scheme of the reaction plane $\gamma P \to \gamma^* P'$ (for TCS) in the γP CM frame and illustration of some of the kinematic variables. Red arrows show the polarization vectors of the photon beam and proton target. Bottom panel: decay angles in the $e^- e^+$ CM frame. ϕ and θ are respectively the azimuthal and polar angles between the e^- direction and the virtual photon direction in the γ^*-P' CM frame.

in fig. 4 the different variables involved. In addition, we display the polarization angle Ψ between the polarization vector of the incoming photon and the scattering plane in the γ^*-p C.M.

The 4-differential unpolarized cross section is then expressed as

$$\frac{\mathrm{d}^4\sigma}{\mathrm{d}Q'^2\mathrm{d}t\mathrm{d}\Omega}(\gamma P \to P'e^+e^-) =$$
$$\frac{1}{(2\pi)^4}\frac{1}{64}\frac{1}{(2mE_\gamma)^2}|T^{\mathrm{BH}} + T^{\mathrm{TCS}}|^2, \qquad (24)$$

where $|T^{\mathrm{BH}} + T^{\mathrm{TCS}}|^2$ is averaged over the target proton helicities and beam polarizations and summed over the final proton helicities.

3 Experimental considerations

The only data for the process $\gamma P \to P'e^-e^+$ which are in the phase space of concern for our study, have been collected and analyzed a few years ago by the CLAS Collaboration using the $\approx 6\,\mathrm{GeV}$ electron beam of Jefferson Lab. The data were actually obtained in "quasi-photoproduction" mode. This means that the scattered

electron from the beam is not detected in CLAS and is considered to be in almost the same direction as the beam-line. This results in very low Q^2 electroproduction, *i.e.* "quasi-photoproduction". This pilot analysis can be found in ref. [23]. The $\approx 6\,\mathrm{GeV}$ beam energy, combined with the $\approx 10^{34}\,\mathrm{cm}^{-2}\,\mathrm{s}^{-1}$ luminosity, allowed to reach maximum Q'^2 values of $3\,\mathrm{GeV}^2$, which corresponds to an invariant mass of the e^+e^- system $M_{e^+e^-}$ of $\approx 1.8\,\mathrm{GeV}$. This is close to the mass of several vector mesons decaying into e^+e^-, in particular the broad $\rho'(1700)$. In order to have a TCS interpretation as clean as possible, it is of course advisable to avoid such resonances which contribute to the process $\gamma P \to P'e^-e^+$. The data analysis of ref. [23] is therefore difficult to interpret in terms of GPDs but it nevertheless demonstrates that the process $\gamma P \to P'e^-e^+$ can be measured at JLab.

The forthcoming JLab energy upgrade to $11\,\mathrm{GeV}$ allows to explore a Q'^2 region between 4 and $9\,\mathrm{GeV}^2$ which corresponds to a $M_{e^+e^-}$ region between 2 and $3\,\mathrm{GeV}$, *i.e.* a vector meson resonance-free region between the ρ' and the J/Ψ. In the case of CLAS12, the upgraded CLAS detector associated to the JLab energy increase, there is also a luminosity gain of a factor 10. These upgrades have led to the first dedicated TCS accepted proposal at JLAB [24]. It will use a similar "quasi-photoproduction" technique as used in the pioneer $6\,\mathrm{GeV}$ analysis. In addition, there will be the improvement of the detection of the low Q^2 scattered electron via a dedicated tagging equipement, supplementing CLAS12. This allows, besides the measurement of unpolarized cross sections, to obtain linearly polarized photons observables, by measuring the azimuthal dependence of the scattered electron. Finally, with a polarized electron beam, which is available at JLab, one can access circularly polarized photons observables. It is therefore expected that in the next few years, numerous $\gamma P \to P'e^-e^+$ data which can lend to GPD interpretation will be available.

We show in fig. 5 the kinematical domain which can be accessed with the upgraded JLab. We display in blue the (ξ, Q'^2) phase space accessible for TCS with an $11\,\mathrm{GeV}$ electron beam, assuming that the real photon is provided by bremsstrahlung of the electron and that its energy is in $E_\gamma \in [5, 11]\,\mathrm{GeV}$. We have applied two cuts: $Q'^2 \in [4, 9]\,\mathrm{GeV}^2$ and $-t \in [0, 1]\,\mathrm{GeV}^2$. The motivations are respectively to stay in the region free of vector mesons resonances and minimize higher twist corrections to the TCS formalism, which grow with $\frac{t}{Q'^2}$. We overlap in red in this same figure the (ξ, Q^2) phase space accessible with an $11\,\mathrm{GeV}$ beam for DVCS. We have applied the cuts: $-t \in [0, 1]\,\mathrm{GeV}^2$, for the same reason as for TCS, and $s > 4\,\mathrm{GeV}^2$ in order to stay above the baryon resonance region.

One notes the large intersection between the DVCS and the TCS phase spaces. Measurements of observables sensitive to GPDs in the common (ξ, Q^2) region by both processes should bring strong constraints on the extraction of GPDs and tests of factorization and universality.

We now present our results for the calculations of the unpolarized cross sections, single-spin asymmetries
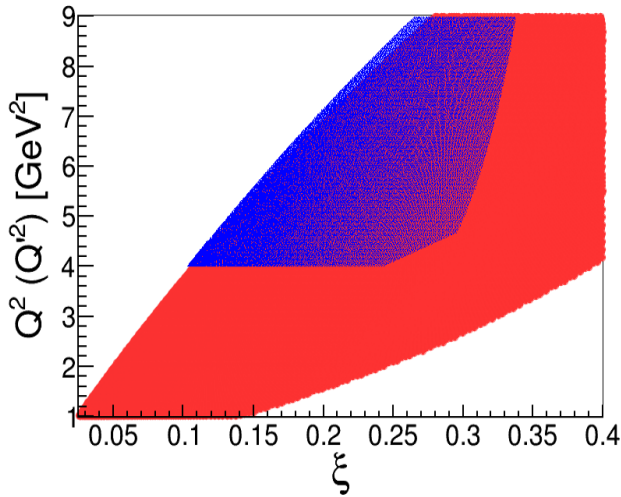
Fig. 5. Kinematical domain accessible as a function of ξ and Q^2 for DVCS (red plain surface) and in ξ and Q'^2 for TCS (blue dotted surface) with an 11 GeV electron beam. For DVCS, the cuts $-t \in [0, 1]\,\text{GeV}^2$ and $s > 4\,\text{GeV}^2$ have been applied and for TCS, the cuts $E_\gamma \in [5, 11]\,\text{GeV}$, $-t \in [0, 1]\,\text{GeV}^2$ and $Q'^2 \in [4, 9]\,\text{GeV}^2$ have been applied.

and double-spin asymmetries, respectively in sects. 4, 5 and 6. In these sections, all calculations will be done in the Bjorken limit and at leading order (we refer the reader to refs. [25–27] for works on next-to-leading-order corrections in α_s to the TCS amplitude). In sect. 7, we will study the effect of keeping the exact kinematics presented in sect. 2.1 and of the gauge invariance restoration prescription described in sect. 2.3.

4 Unpolarized cross section

We discuss in this section the unpolarized cross section of the $\gamma P \to P'e^+e^-$ process, which therefore includes the BH and TCS processes. The upper panel of fig. 6 shows our calculation of the ϕ-dependence of the 4-fold differential cross section $\frac{\mathrm{d}\sigma_{\text{BH}}}{\mathrm{d}Q'^2\,\mathrm{d}t\,\mathrm{d}\phi\,\mathrm{d}(\cos\theta)}$ at $\xi = 0.2$, $-t = 0.4\,\text{GeV}^2$, $Q'^2 = 7\,\text{GeV}^2$ and for different θ values. The ϕ-shape is strongly dependent on the θ value. As θ tends to $0°$, the ϕ distribution peaks towards $\phi = 180°$ and as θ tends to $180°$, the ϕ-distribution peaks towards $\phi = 0°$ (or $360°$). There is a smooth transition between these two singularities for the intermediate θ values. For instance, at $\theta = 90°$, the calculation shows only two small "bumps" at $\phi = 0°$ and $\phi = 180°$.

These particular shapes are due to the BH process and its singularities. Indeed, in the BH diagrams of fig. 3, when the electron (positron) is emitted in the direction of the initial photon, *i.e.* $\theta = 0°$ ($\theta = 180°$), the propagator of the positron (electron) becomes singular and creates a peak in the ϕ distribution at $\phi = 180°$ ($\phi = 0°$). Intuitively, $\theta = 0°$ ($\theta = 180°$) forces all particles to be in the same plane, *i.e.* $\phi = 180°$ ($\phi = 0°$). The kinematics $\theta = 0°$, *i.e.* the electron is in the direction of the photon
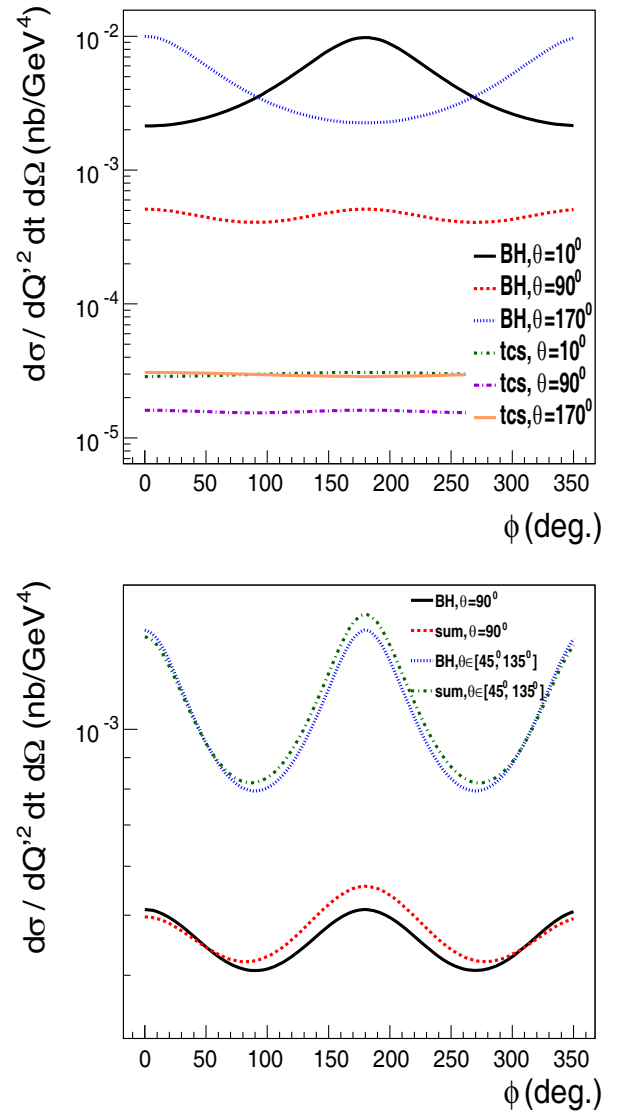
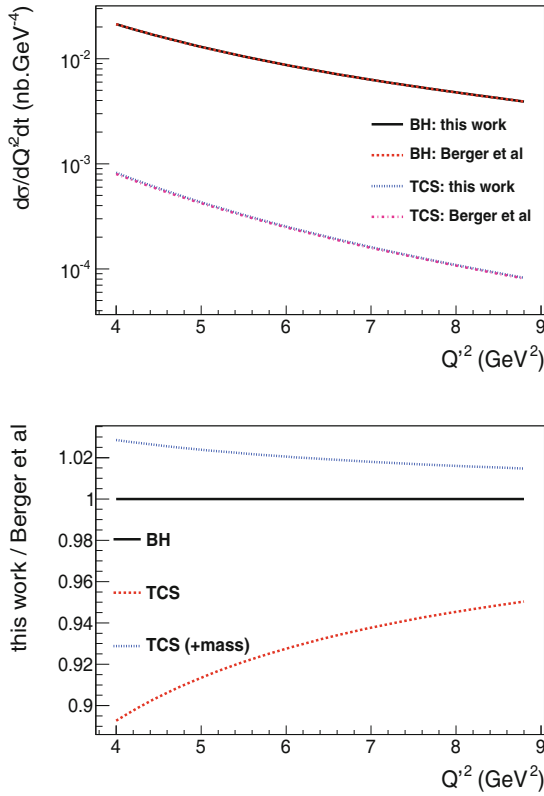**Fig. 6.** Top panel: unpolarized cross section $\frac{\mathrm{d}\sigma}{\mathrm{d}Q'^2\,\mathrm{d}t\,\mathrm{d}\phi\,\mathrm{d}(\cos\theta)}$ for the process $\gamma P \to P'e^+e^-$, for BH alone and TCS alone as a function of ϕ, at $\xi = 0.2$, $-t = 0.4\,\text{GeV}^2$, $Q'^2 = 7\,\text{GeV}^2$ for different fixed θ values: $10°$, $90°$, $170°$. Bottom panel: unpolarized cross section $\frac{\mathrm{d}\sigma}{\mathrm{d}Q'^2\,\mathrm{d}t\,\mathrm{d}\phi\,\mathrm{d}(\cos\theta)}$ for the process $\gamma P \to P'e^+e^-$, for BH alone and for BH+TCS as a function of ϕ, at $\xi = 0.2$, $-t = 0.4\,\text{GeV}^2$, $Q'^2 = 7\,\text{GeV}^2$ for $\theta = 90°$ and for θ integrated over $[\pi/4, 3\pi/4]$.

beam, corresponds to $\phi = 180°$ because the virtual photon is emitted by the positron, not the electron (see fig. 6).

We display also in the upper panel of fig. 6 the contribution of TCS alone. In this calculation, we have used only the GPD H. The inclusion of the other GPDs barely changes the curves. In contrast to the BH, the TCS is almost flat in ϕ for all θ values. It is clear that the process $\gamma P \to P'e^+e^-$ is largely dominated by the BH. There is never less than an order of magnitude between BH and TCS.

In the lower panel of fig. 6, we compare our calculations for BH+TCS and for BH alone at $\theta = 90°$. This is the

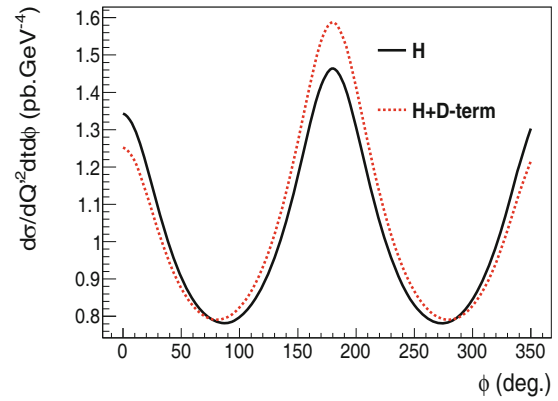**Fig. 8.** The three-fold differential cross section $\mathrm{d}\sigma/\mathrm{d}Q'^2\mathrm{d}t\mathrm{d}\phi$ as a function of ϕ with (red dashed curve) and without (black solid curve) the D-term, calculated at $\xi = 0.2$, $-t = 0.4\,\mathrm{GeV}^2$ and with θ integrated over $[\frac{\pi}{4}, \frac{3\pi}{4}]$.

Fig. 7. Top panel: the two-fold differential cross section $\mathrm{d}\sigma/$ $\mathrm{d}Q'^2\mathrm{d}t$ for BH (highest curves) and TCS (lowest curves) as a function of Q'^2 for $\xi = 0.2$ and $-t = 0.4\,\mathrm{GeV}^2$. The calculations have been integrated over $\phi \in [0, 2\pi]$ and $\theta \in [\frac{\pi}{4}, \frac{3\pi}{4}]$. The solid curves are our calculations while the dashed curves are from ref. [5]. Bottom panel: ratio of our calculations to those of ref. [5]. For the TCS process, the blue dotted curve contains the nucleon mass term in the phase space factor in the calculation of ref. [5] while the red dashed curve does not.

value of the θ angle for which one is far from the two BH singularities and for which the difference between the two calculations and therefore the sensitivity to TCS should be the most pronounced. The ratio between the two curves is of the order of 30% at $\phi = 180°$. As one gets closer to one of the two BH singularities, the two curves BH and BH+TCS are essentially indistinguishable and there is no sensitivity to TCS.

Also, we show in the lower panel of fig. 6 our calculations of BH+TCS (and of BH alone) for θ integrated over the range $[\pi/4, 3\pi/4]$. In order to maximize count rates, from an experimental point of view, it is interesting to integrate over θ. We still have a sensitivity to TCS, however it is of the order of 5%, *i.e.* lesser than at fixed $\theta = 90°$: the integration over θ dilutes the sensitivity to TCS.

We display in the top panel of fig. 7 the Q'^2-dependence, at $\xi = 0.2$ and $-t = 0.4\,\mathrm{GeV}^2$, of $\mathrm{d}\sigma/\mathrm{d}Q'^2\mathrm{d}t$ for the BH and TCS processes. The 2-fold cross section has been integrated over the decay angles: $\phi \in [0, 2\pi]$ and $\theta \in [\frac{\pi}{4}, \frac{3\pi}{4}]$. We also display in this figure the results of the analytical formulaes of ref. [5]. For TCS, we have of course used the same GPD parameterization for both calculations (only H in this case).

In order to better appreciate the comparison, we display in the bottom panel of fig. 7 the ratios of our calculations to those of ref. [5]. The agreement is excellent for the BH process, as it should, since there was no approximation done in the derivation of the analytical formula for this process in ref. [5]. For TCS, we show two curves for the ratio. Indeed, in ref. [5], in the analytical formula for the TCS process, the nucleon mass was neglected in the phase space factor, *i.e.* the cross section is proportional to $\frac{1}{s^2}$ rather than $\frac{1}{s - m^{2^2}}$ (this is not the case for the BH process where the phase space factor is exact in ref. [5]). In the bottom panel of fig. 7, we plot the TCS cross section of ref. [5] with (blue dotted curve) and without (red dashed curve) the nucleon mass term in the phase space factor. In this way, one can distinguish the differences between the two calculations originating from the trivial phase space factor from those, more subtle, coming from the TCS amplitude. It is seen in this figure that at the lowest Q'^2 values and at the presently considered kinematics, the difference in the cross section calculations depending on the prescription taken for the phase space factor can reach more than 10%. In both cases, it is also seen that the difference between the Berger *et al.*'s calculations and ours diminishes as Q'^2 increases, as expected since terms of the order of $\frac{m^2}{Q'^2}$ were dropped in the TCS analytical formula of ref. [5].

To end this section concerning the unpolarized cross section, we show in fig. 8 the influence of the D-term on the three-fold differential cross section $\mathrm{d}\sigma/\mathrm{d}Q'^2\mathrm{d}t\mathrm{d}\phi$, calculated for $\xi = 0.2$, $-t = 0.4\,\mathrm{GeV}^2$ and with θ integrated over $[\frac{\pi}{4}, \frac{3\pi}{4}]$. It modifies the amplitude of the cross section at $\phi = 0°$ and $\phi = 180°$ by about 10%.

5 Single-spin asymmetries

We now turn to the single-spin asymmetries: beam or target. Photons beams can be polarized linearly or circularly. Target polarization vectors can be oriented along the x-, y- or z-axis in the $\gamma P \rightarrow \gamma^* P'$ plane (see fig. 4). For
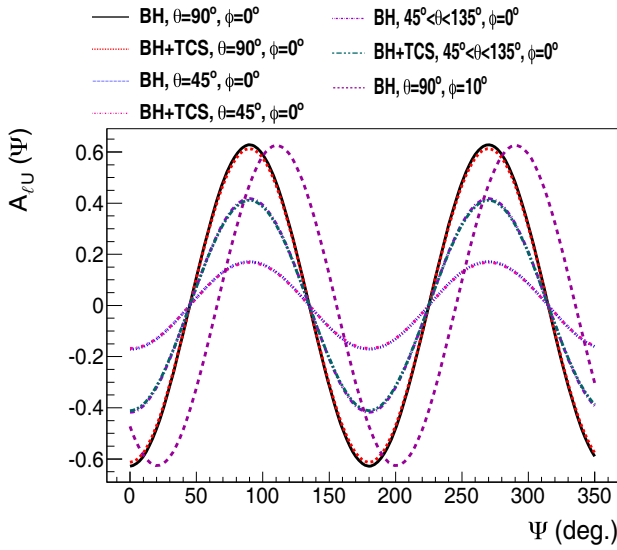
Fig. 9. $A_{\ell U}$ asymmetry as a function of Ψ for BH and for BH+TCS (only GPD H contribution) at $\xi = 0.2$, $-t = 0.4\,\mathrm{GeV}^2$, $Q'^2 = 7\,\mathrm{GeV}^2$ and for different sets of θ and ϕ angles.

polarization observables, we will calculate spin asymmetries and, following notations used for DVCS, we will tag them A_{ij}, *i.e.* with two indices i and j. The first index i refers to the polarization type of the beam: U for an unpolarized beam, $\odot$ for a circularly polarized beam and ℓ for a linearly polarized beam. The second index j refers to the polarization of the target and can take the values U, x, y or z, with obvious meanings. In this section, dedicated to single-polarization observables, we will therefore consider successively the five independent asymmetries $A_{\ell U}$, $A_{\odot U}$, A_{Ux}, A_{Uy} and A_{Uz}.

In this section, as well as in the following one on double-spin asymmetries, our calculations are carried out for 100% polarisation. Circularly polarized photons, linearly polarized photons and proton polarized targets with high degrees of polarization (between 60% and 90%) have been obtained and used these past years almost routinely at JLab (see for instance ref. [28]).

5.1 Linearly polarized photons

We introduce the angle Ψ between the polarization vector of the photon and the plane spanned by the photon beam and the (e^+e^-) system, which contains the x-axis (see fig. 4). Then, we define

$$A_{\ell U}(\Psi) = \frac{\sigma(\Psi) - \sigma(\Psi + \pi/2)}{\sigma(\Psi) + \sigma(\Psi + \pi/2)}, \qquad (25)$$

where the σ's stand for the 4-fold differential cross sections $\frac{\mathrm{d}\sigma}{\mathrm{d}Q'^2\,\mathrm{d}t\,\mathrm{d}\phi\,\mathrm{d}(\cos\theta)}$.

We display in fig. 9 the Ψ-dependence of $A_{\ell U}$ for $\xi = 0.2$, $-t = 0.2\,\mathrm{GeV}^2$, $Q'^2 = 7\,\mathrm{GeV}^2$ for $\theta = 45°$, $\theta = 90°$ and θ integrated over $[\pi/4, 3\pi/4]$ and $\phi = 0°$ and $\phi = 10°$. The approximate shape of the asymmetry
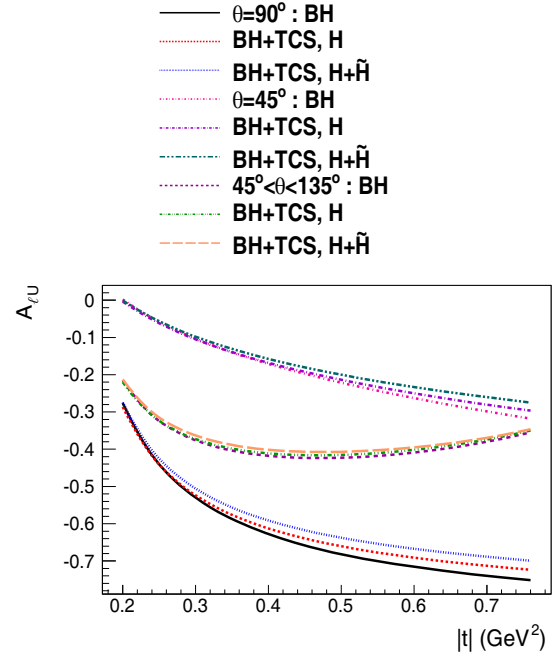
Fig. 10. $A_{\ell U}$ asymmetry as a function of t for $\xi = 0.2$, $Q'^2 = 7\,\mathrm{GeV}^2$, $\Psi = 0°$, $\phi = 0°$ and $\theta = 45°$, $\theta = 90°$ and $\theta \in [\pi/4, 3\pi/4]$.

is a $\cos(2\Psi)$ which is reminiscent of the modulation which is predicted for the so-called Σ asymmetry in single meson photoproduction. This $\cos(2\Psi)$ modulation appears explicitly in the analytical expressions of ref. [6].

We note that the BH alone produces an asymmetry. It is actually the dominant contribution. The TCS produces only variations of the amplitude at the percent level around the BH, making this observable not very favorable to study TCS and GPDs. The amplitude and phase of the asymmetry depend strongly on the decay angles: it is the strongest as θ approaches $90°$ and the phase increases as ϕ increases. This phase shift due to ϕ is also apparent in ref. [6].

In fig. 9, we have used only the contribution of the H GPD for TCS. In fig. 10, we show the t-dependence of the $A_{\ell U}$ asymmetry for BH alone, BH+TCS (with only H) and BH+TCS (with $H + \tilde{H}$). Calculations have been done for $\xi = 0.2$, $Q'^2 = 7\,\mathrm{GeV}^2$, $\phi = 0°$, $\Psi = 180°$ and for $\theta = 45°$, $\theta = 90°$ and θ integrated over $[\pi/4, 3\pi/4]$. Depending on t, we notice some sensitivity of the $A_{\ell U}$ observable to the GPDs H and $\tilde{H}$.

In fig. 11, we show the peculiar ϕ-dependence of $A_{\ell U}$ at $\Psi = 0°$ at our standard kinematics. We also show the (small) influence of the D-term.

We finally note that the ϕ and Ψ-dependences are not completely independent. As Ψ is defined along the incoming real photon direction and ϕ along the outgoing virtual photon direction, the polar angle between the outgoing and incoming photons intervene in the relation between these two dependencies. We have shown the two dependencies which, according to the particular experimental needs and/or kinematics, might be both useful.
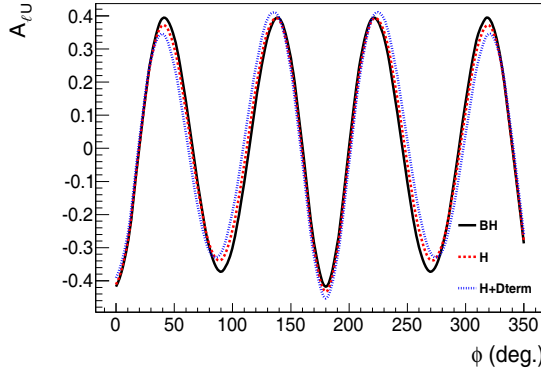
Fig. 11. $A_{\ell U}$ asymmetry as a function of ϕ for $\xi = 0.2$, $Q'^2 = 7\,\mathrm{GeV}^2$, $-t = 0.4\,\mathrm{GeV}^2$, $\Psi = 0°$ and $\theta \in [\pi/4, 3\pi/4]$. The black solid curve corresponds to BH only, the red dashed curve to BH+TCS with only the GPD H contribution and the blue dotted curve to BH+TCS with the GPD H and the D-term contributions.

5.2 Circularly polarized photons

We define:

$$A_{\odot U} = \frac{\sigma^+ - \sigma^-}{\sigma^+ + \sigma^-}, \qquad (26)$$

where $\sigma^{\pm}$ stand for the 4-fold differential cross sections $\frac{\mathrm{d}\sigma}{\mathrm{d}Q'^2\,\mathrm{d}t\,\mathrm{d}\phi\,\mathrm{d}(\cos\theta)}$ for the two photon spin states, right and left polarized.

We display in fig. 12 (top panel) our results for $A_{\odot U}$ as a function of ϕ at $Q'^2 = 7\,\mathrm{GeV}^2$, $\xi = 0.2$, $-t = 0.4\,\mathrm{GeV}^2$ for $\theta = 45°$, $90°$ and θ integrated over $[45°, 135°]$. The TCS is calculated here with only the H GPD. In all kinematics, we obtain a $\sin(\phi)$ shape with a significant amplitude, up to $\approx 25\%$. We observe that the BH does not produce any asymmetry. Any signal therefore reflects a contribution from TCS. This is due to the fact that, as was shown in ref. [5], this observable is sensitive to the imaginary part of the amplitude and that the BH amplitude is purely real. The amplitude of the asymmetry depends on θ. It is maximal for $\theta = 90°$, where BH is minimal and it decreases as θ tends to $\theta = 0°$ (or $180°$). Since the BH does not produce on its own an asymmetry, one sees that the integration over θ does not strongly reduce the signal. Such integration allows to maximize count rates.

In fig. 12 (top panel), we also compare our results to those of ref. [5]. In all cases, our calculations produce amplitudes a few percents larger. This might be attributed to some mass correction terms to the TCS amplitude which are present in our calculation and not in ref. [5].

Figure 12 (bottom panel) shows the $A_{\odot U}$ asymmetry for θ integrated over $[45°, 135°]$ using different GPDs parametrizations for TCS.

In fig. 13, we show for $\xi = 0.2$, $Q'^2 = 7\,\mathrm{GeV}^2$, $\phi = 90°$ and θ integrated over $[45°, 135°]$, the t-dependence of $A_{\odot U}$ and its sensitivity to different GPDs. We notice that the magnitude of $A_{\odot U}$ increases with $|t|$ and that there is a sensitivity of this observable to all four GPDs, especially at large $|t|$. We also display in this figure our calculation with the factorized ansatz for the t-dependence of the H
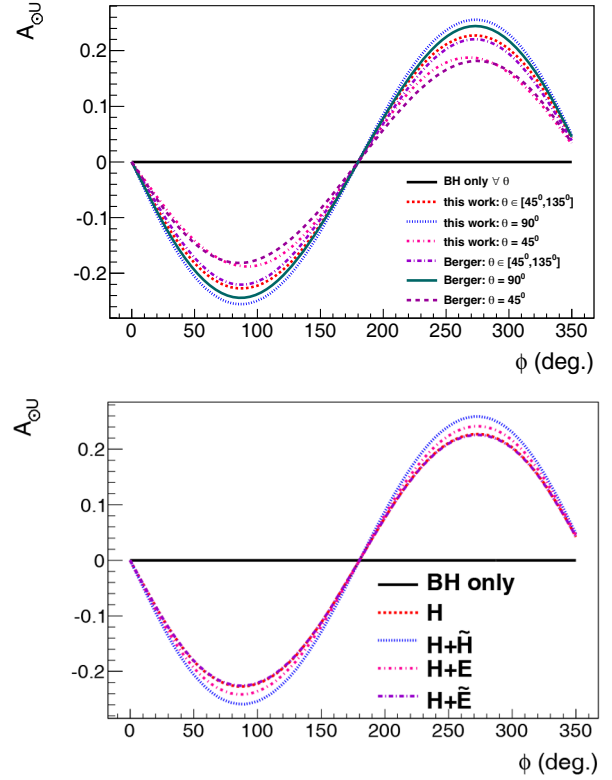
Fig. 12. Top panel: The $A_{\odot U}$ asymmetry as a function of ϕ for $\theta = 45°$, $\theta = 90°$ and $\theta \in [45°, 135°]$. The TCS is calculated here with only the H GPD. We compare our calculations to those of ref. [5]. Bottom panel: The $A_{\odot U}$ for $\theta \in [45°, 135°]$ using differents GPDs parametrizations for TCS. The calculations are done for $Q'^2 = 7\,\mathrm{GeV}^2$, $\xi = 0.2$, $-t = 0.4\,\mathrm{GeV}^2$.

GPD in order to illustrate the model-dependence of our results.

5.3 Polarized targets

We define

$$A_{Ui} = \frac{\sigma^+ - \sigma^-}{\sigma^+ + \sigma^-}, \qquad (27)$$

where $\sigma^{\pm}$ stands for the four-fold differential cross sections $\frac{\mathrm{d}\sigma}{\mathrm{d}Q'^2\,\mathrm{d}t\,\mathrm{d}\phi\,\mathrm{d}(\cos\theta)}$ for the two target spin orientations $+$ and $-$ along the axis $i = x, y$ or z.

We show in fig. 14 our results for the ϕ-dependence of A_{Ux}, A_{Uy} and A_{Uz} for $Q'^2 = 7\,\mathrm{GeV}^2$, $\xi = 0.2$, $-t = 0.4\,\mathrm{GeV}^2$ for θ integrated over $[\frac{\pi}{4}, \frac{3\pi}{4}]$. Like for $A_{\odot U}$, it is advantageous to integrate over θ, in order to maximize count rates, since the signal is barely reduced. The TCS is calculated with different GPD contributions. We observe $\sin\phi$ or $\cos\phi$ shapes with amplitudes between 10 and 15%. Like for $A_{\odot U}$, the BH does not produce any asymmetry and any non-zero asymmetry directly reflects the strength of GPDs.
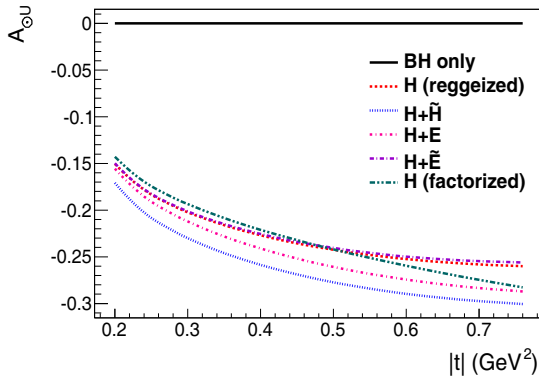
Fig. 13. The $A_{\odot U}$ asymmetry as a function of t for BH+TCS at $\xi = 0.2$, $Q'^2 = 7\,\mathrm{GeV}^2$, $\phi = 90°$ and θ integrated over $[45°, 135°]$. TCS is calculated with different GPD contributions.

We show in fig. 15 the t-dependence of A_{Ux}, A_{Uy} and A_{Uz} at $\phi = 90°$, $0°$ and $90°$ respectively, for the kinematics $\xi = 0.2$, $Q'^2 = 7\,\mathrm{GeV}^2$ and θ integrated over $[\frac{\pi}{4}, \frac{3\pi}{4}]$. In this figure, TCS is calculated with different GPDs. Depending on the value of t, the three asymmetries are sensitive to the GPDs H, $\tilde{H}$ and E in various proportions. We also display in this figure our calculation with the factorized ansatz for the t-dependence of the H GPD in order to illustrate the model-dependence of our results.

6 Double-spin asymmetries

We define the double-spin asymmetries,

$$A_{ij} = \frac{(\sigma^{++} + \sigma^{--}) - (\sigma^{+-} + \sigma^{-+})}{\sigma^{++} + \sigma^{--} + \sigma^{+-} + \sigma^{-+}}, \qquad (28)$$

where $\sigma^{\pm\pm}$ stand for the four-fold differential cross sections $\frac{\mathrm{d}\sigma}{\mathrm{d}Q'^2\,\mathrm{d}t\,\mathrm{d}\phi\,\mathrm{d}(\cos\theta)}$ for the two photon beam spin states $+$ and $-$ (first index) and the two target spin orientations $+$ and $-$ (second index) along the target polarization axis. The first index of A refers to the polarization nature of the photon beam ($i = \ell$ for a linear polarization and $i = \odot$ for a circular polarization) and the second index refers to the axis polarization of the target $j = x, y$ or z. We present and discuss in the two following subsections our results for $A_{\odot j}$ and $A_{\ell j}$.

6.1 Circularly polarized photons and polarized target

Figure 16 shows our results for $A_{\odot x}$, $A_{\odot y}$ and $A_{\odot z}$, from left to right, as a function of ϕ at the kinematics $\xi = 0.2$, $-t = 0.4\,\mathrm{GeV}^2$, $Q'^2 = 7\,\mathrm{GeV}^2$. The top row shows the result of our calculations for θ integrated over $[\frac{\pi}{4}, \frac{3\pi}{4}]$ with different GPD contributions to the TCS amplitude. The bottom row shows the same observables with only the GPD H contribution for different θ angle sets.

One notes that the BH process alone produces asymmetries in all cases. The ϕ-shapes of the asymmetries are

complex and very dependent on θ. Also, in contrast to the single-spin asymmetries that we studied in the previous section, the ϕ-shapes are also very dependent on the specific GPDs entering the TCS process. One notes in particular important sensitivities to the H, $\tilde{H}$, $\tilde{E}$ GPDs as well as to the D-term. Furthermore, one also notes the sensitivity of these double-polarization observables to the ansatz used for the t-dependence.

Figure 17 shows the t-dependence of the double-spin asymmetries $A_{\odot x}$, $A_{\odot y}$ and $A_{\odot z}$ at $\phi = 0°$, $\phi = 90°$ and $\phi = 0°$ respectively, at the kinematics $\xi = 0.2$, $Q'^2 = 7\,\mathrm{GeV}^2$ and θ integrated over $[\pi/4, 3\pi/4]$. We also display in this figure our calculation with the factorized ansatz for the t-dependence of the H GPD in order to illustrate the model-dependence of our results. The change of sign for $A_{\odot y}$ for the factorized ansatz compared to the Reggeized ansatz is in particular remarkable. As can be seen in the top panel of fig. 16, this is due to the fact that the factorized model crosses the "zero" line before $\phi = 90°$ while the Reggeized model crosses it after, thus producing respectively positive and negative $A_{\odot y}$'s at $\phi = 90°$.

6.2 Linearly polarized photons and polarized target

Figure 18 shows our results for the double-spin asymmetries $A_{\ell x}$, $A_{\ell y}$ and $A_{\ell z}$, from left to right, as a function of ϕ at the kinematics $\xi = 0.2$, $-t = 0.4\,\mathrm{GeV}^2$, $Q'^2 = 7\,\mathrm{GeV}^2$ with θ integrated over $[\frac{\pi}{4}, \frac{3\pi}{4}]$.

One notes that the BH process alone produces a null asymmetry in all cases, making this double-spin asymmetry particularly favorable to study TCS and GPDs. $A_{\ell y}$ is mostly sensitive to the GPD H contribution while $A_{\ell x}$ and $A_{\ell z}$ show a sensitivity to the GPD $\tilde{H}$ as well.

7 Corrections to the leading-twist calculations

We evaluate in this final section two types of higher-twist corrections: keeping the exact kinematics presented in sect. 2.1, *i.e.* $|\tilde{\xi}| \neq |\xi| \neq |\tilde{\xi}'| \neq |\xi'|$, and adding the gauge correction term of sect. 2.3 to the TCS tensor.

Figure 19 shows the Q'^2-dependence and the $|t|$-dependence of the ratio of the 2-fold cross differential cross sections $\mathrm{d}\sigma/\mathrm{d}t\mathrm{d}Q'^2$ for Bethe-Heitler and for TCS (integrated over the decay angles: $\phi \in [0, 2\pi]$ and $\theta \in [\frac{\pi}{4}, \frac{3\pi}{4}]$) calculated with the gauge invariance restoration term (dot-dashed curve for TCS) and with the exact kinematics (dotted curve for TCS) to the asymptotic limit (*i.e.* Bjorken limit) calculation that we have presented so far. The calculation has been carried out for $\xi = 0.1$ and at $-t = 0.4\,\mathrm{GeV}^2$ (left panel) or at $Q'^2 = 7\,\mathrm{GeV}^2$ (right panel). One sees that these ratios tend to 1 as Q'^2 increases and as $|t|$ decreases, as expected. The effects of these corrections in the domains of current interest, cov-
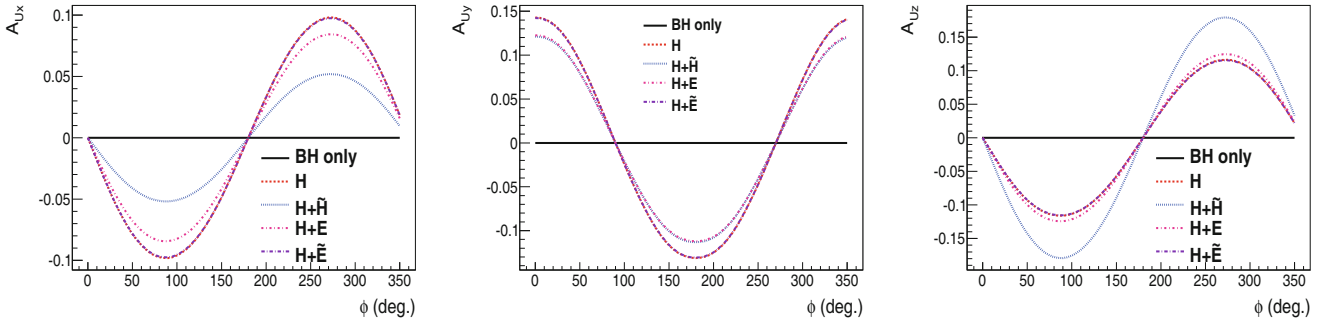
Fig. 14. The A_{Ux} (left panel), A_{Uy} (central panel) and A_{Uz} (right panel) asymmetries as a function of ϕ for $\xi = 0.2$, $Q'^2 = 7\,\mathrm{GeV}^2$, $-t = 0.4\,\mathrm{GeV}^2$ and for θ integrated over $[\frac{\pi}{4}, \frac{3\pi}{4}]$. The TCS is calculated with different GPDs contributions.
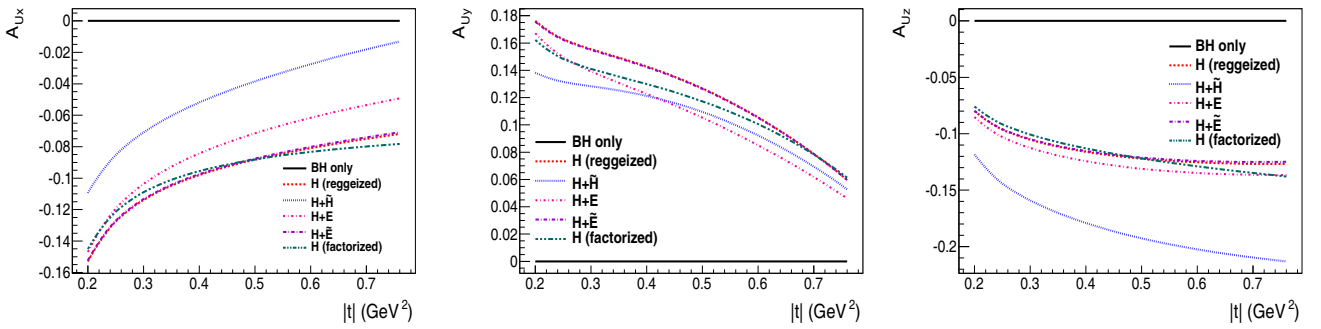

Fig. 15. The A_{Ux} (left panel), A_{Uy} (central panel) and A_{Uz} (right panel) asymmetries as a function of t, at $\phi = 90°$, $0°$ and $90°$ respectively, and for $\xi = 0.2$, $Q'^2 = 7\,\mathrm{GeV}^2$, $-t = 0.4\,\mathrm{GeV}^2$ and θ integrated over $[\frac{\pi}{4}, \frac{3\pi}{4}]$. TCS is calculated with different GPD contributions.
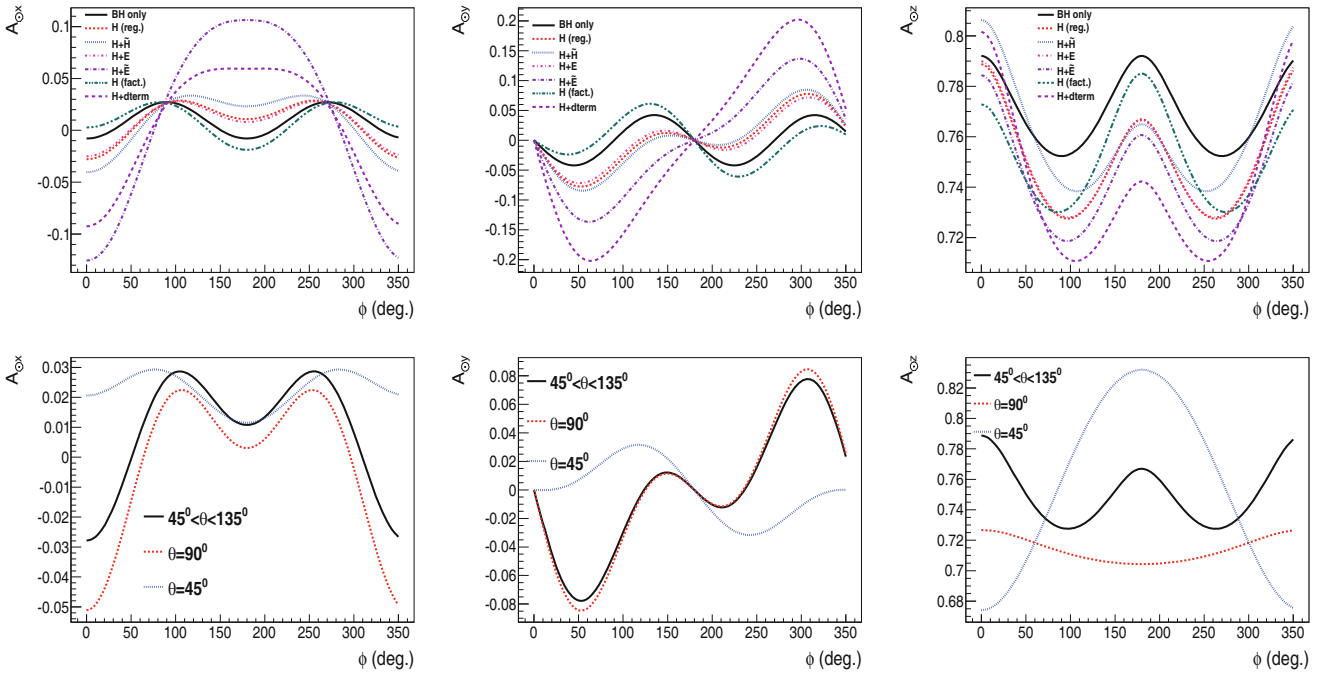

Fig. 16. Circularly polarized beam-target double-spin asymmetries as a function of ϕ at $\xi = 0.2$, $-t = 0.4\,\mathrm{GeV}^2$ and $Q'^2 = 7\,\mathrm{GeV}^2$. Left column: $A_{\odot x}$. Central column: $A_{\odot y}$. Right column: $A_{\odot z}$. In the top row panels, θ integrated over $[\frac{\pi}{4}, \frac{3\pi}{4}]$ and the calculations are done for different GPD contributions to the TCS process. In the bottom row panels, the calculations are done for different θ angles: $\theta = 90°$ (red dashed curve), $\theta = 45°$ (blue dotted curve) and θ integrated over $[\frac{\pi}{4}, \frac{3\pi}{4}]$ (black solid curve) and with the GPD H (Reggeized) contribution only.
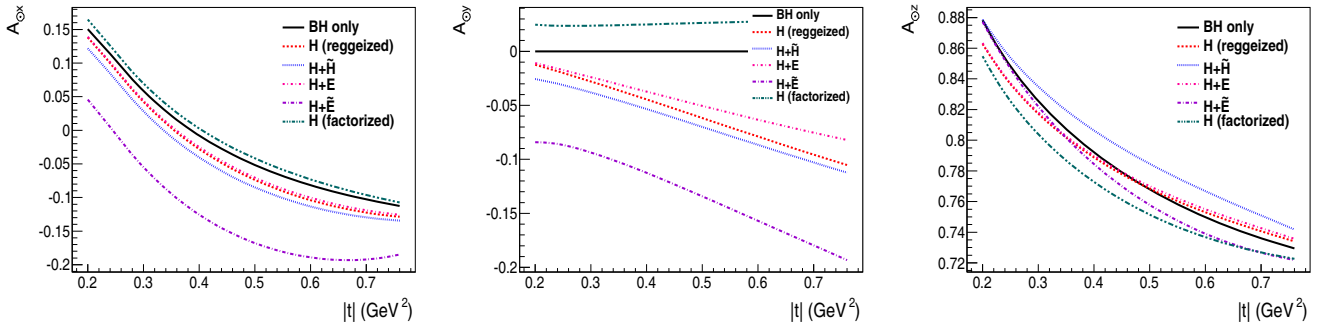
Fig. 17. Circularly polarized beam-target double-spin asymmetries as a function of t. Left: $A_{\odot x}$. Center: $A_{\odot y}$. Right: $A_{\odot z}$. Calculations are done at the kinematics: $\xi = 0.2$, and $Q'^2 = 7\,\mathrm{GeV}^2$ and $\phi = 0°$ ($A_{\odot x}$), $\phi = 90°$ ($A_{\odot y}$) and $\phi = 0°$ ($A_{\odot z}$). θ is integrated over $[\frac{\pi}{4}, \frac{3\pi}{4}]$ in these calculations.
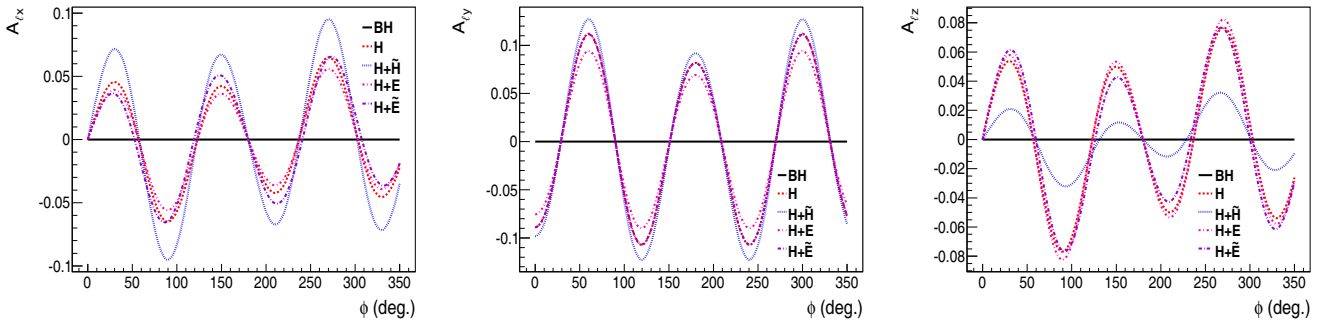

Fig. 18. Linearly polarized beam-target double-spin asymmetries as a function of ϕ at $\xi = 0.2$, $-t = 0.4\,\mathrm{GeV}^2$ and $Q'^2 = 7\,\mathrm{GeV}^2$ and θ integrated over $[\frac{\pi}{4}, \frac{3\pi}{4}]$ for different GPD contributions. Left column: $A_{\ell x}$. Central column: $A_{\ell y}$. Right column: $A_{\ell z}$.
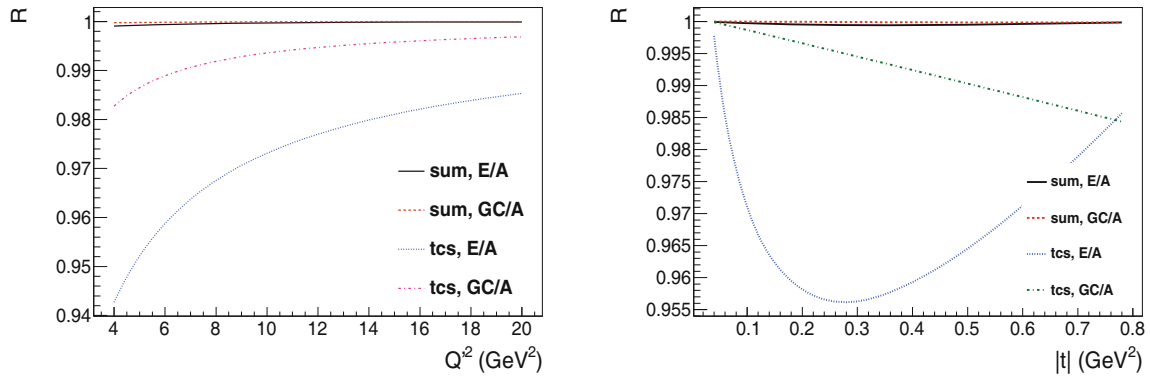
Fig. 19. Q'^2-dependence (left panel) and $|t|$-dependance (right panel) of the ratio of the 2-fold cross differential cross sections $\mathrm{d}\sigma/\mathrm{d}t\mathrm{d}Q'^2$ of Bethe-Heitler and of TCS (integrated over the decay angles: $\phi \in [0, 2\pi]$ and $\theta \in [\frac{\pi}{4}, \frac{3\pi}{4}]$) calculated with the gauge invariance restoration term (dot-dashed curve for TCS: gauge invariant/asymptotic) and with the exact kinematics (dotted curve for TCS: "exact"/asympototic) to the asymptotic limit (*i.e.* Bjorken limit) calculation. The calculation has been carried out for $\xi = 0.1$, θ is integrated over $[\pi/4, 3\pi/4]$, ϕ is integrated over $[0, 2\pi]$ and at $-t = 0.4\,\mathrm{GeV}^2$ (left panel) or at $Q'^2 = 7\,\mathrm{GeV}^2$ (right panel).

ered in this figure, are of the order of a few percents for TCS. The exact kinematic corrections are more important (always less than 6% though) than the gauge invariance restoring corrections. We show in fig. 20 that the impact of these corrections on the asymmetries that we discussed earlier is of the order of 0.1% to 1% and do not affect the conclusions that we drew earlier.

The kinematically higher twist corrections as well as the higher-twist gauge correction terms considered here are of course only a part of the higher-twist corrections and can be improved upon. In particular, a next step would involve a full treatment of target mass corrections to twist-4 accuracy, as was done for the DVCS process in ref. [29].
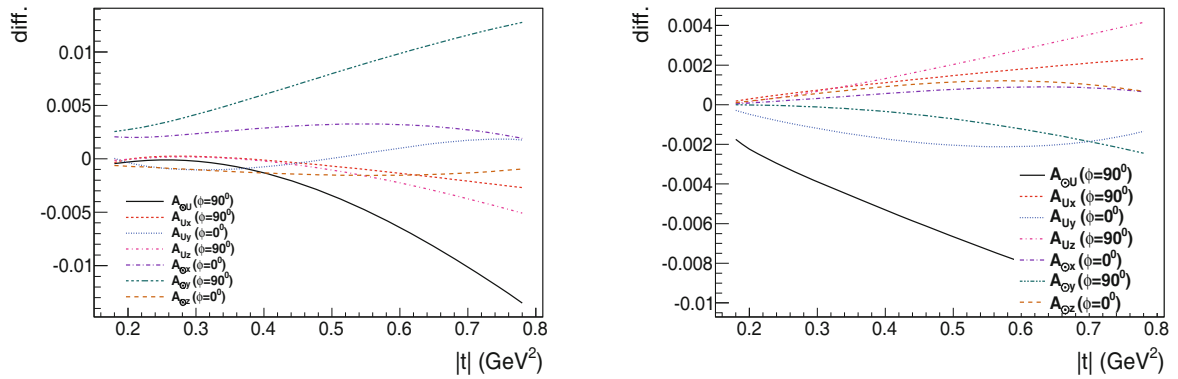
Fig. 20. Difference of the single- and double-spin asymmetries (circularly polarized photon) as a function of $|t|$ before and after the corrections. Left panel: with the exact kinematic compared to the asymptotic limit. Right panel: with the gauge invariance restoration term compared to the asymptotic limit. The calculations have been carried out for $\xi = 0.2$, $-t = 0.4\,\text{GeV}^2$, $Q'^2 = 7\,\text{GeV}^2$ and θ has been integrated over $[\pi/4, 3\pi/4]$. The different ϕ angles are indicated on the figure.

8 Conclusion

In this work, we have studied the $\gamma P \rightarrow P'e^+e^-$ process in terms of GPDs in a regime where one can expect to access them. We have presented our derivations of the TCS and BH amplitudes both contributing to the $\gamma P \rightarrow P'e^+e^-$ process and calculated all unpolarized, single-beam, single-target and double-spin beam-target observables.

We show that, since the TCS process is lower by several factors in the unpolarized cross section compared to the BH process, it is judicious to measure spin asymmetries which reveal a more direct sensitivity to GPDs. In particular, the BH process alone does not produce any signal for the target single-spin asymmetries, for the circularly polarized beam single-spin asymmetries and for the linearly polarized photons and polarized target double-spin asymmetries. These observables are therefore particularly favorable to directly measure GPD strength. We have shown in general that the various single- and double-polarization observables that we have calculated show different sensitivities to the four GPDs, which should ultimately allow to disentangle them with some adequate GPD fitting algorithms. We also provided first estimations of higher-twist contributions such as keeping the exact kinematics and including a gauge invariance restoring term. The effects are at the level of a few percent on cross sections and spin asymmetries.

A rich new experimental TCS program can be envisioned with the forthcoming JLab energy upgrade, which would complement the DVCS program already approved in order to access GPDs. All of the TCS observables that we calculated in this work should be measurable and can serve as a basis for developing experimental proposals. This work might also find some applications at higher energies, like at hadron colliders, such as LHC and RHIC, in ultraperipheral collisions [30] or at the projected electron-ion collider EIC [31].

References

1. K. Goeke, M.V. Polyakov, M. Vanderhaeghen, Prog. Part. Nucl. Phys. **47**, 401 (2001).
2. M. Diehl, Phys. Rep. **388**, 41 (2003).
3. A.V. Belitsky, A.V. Radyushkin, Phys. Rep. **418**, 1 (2005).
4. M. Guidal, H. Moutarde, M. Vanderhaeghen, Rep. Prog. Phys. **76**, 066202 (2013).
5. E.R. Berger, M. Diehl, B. Pire, Eur. Phys. J. C **23**, 675 (2002).
6. A.T. Goritschnig, B. Pire, J. Wagner, arXiv:1404.0713 [hep-ph].
7. X. Ji, Phys. Rev. Lett. **78**, 610 (1997).
8. X. Ji, Phys. Rev. D **55**, 7114 (1997).
9. M. Vanderhaeghen, P.A.M. Guichon, M. Guidal, Phys. Rev. Lett. **80**, 5064 (1998).
10. M. Vanderhaeghen, P.A.M. Guichon, M. Guidal, Phys. Rev. D **60**, 094017 (1999).
11. M. Guidal, M.V. Polyakov, A.V. Radyushkin, M. Vanderhaeghen, Phys. Rev. D **72**, 054013 (2005).
12. A.V. Radyushkin, Phys. Rev. D **59**, 014030 (1999).
13. A.V. Radyushkin, Phys. Lett. B **449**, 81 (1999).
14. D. Mueller, D. Robaschik, B. Geyer, F.M. Dittes, J. Horejsi, Fortsch. Phys. **42**, 101 (1994).
15. M.V. Polyakov, C. Weiss, Phys. Rev. D **60**, 114017 (1999).
16. P.A.M. Guichon, M. Vanderhaeghen, Prog. Part. Nucl. Phys. **41**, 125 (1998).

17. I.V. Anikin, B. Pire, O.V. Teryaev, Phys. Rev. D **62**, 071501 (2000).
18. A.V. Belitsky, D. Mueller, Nucl. Phys. B **589**, 611 (2000).
19. A.V. Radyushkin, C. Weiss, Phys. Rev. D **63**, 114012 (2001).
20. Jefferson Lab Hall A Collaboration (O. Gayou *et al.*), Phys. Rev. Lett. **88**, 092301 (2002).
21. E.J. Brash, A. Kozlov, S. Li, G.M. Huber, Phys. Rev. C **65**, 051001 (2002).
22. A1 Collaboration (J.C. Bernauer *et al.*), Phys. Rev. C **90**, 015206 (2014).
23. R. Paremuzyan, *Time-like Compton Scattering*, PhD thesis, Yerevan Institute (2010).
24. CLAS Collaboration (I. Albayrak *et al.*), *Jefferson Lab PAC 39 Proposal, Timelike Compton Scattering and J/Ψ photoproduction on the proton in e^+e^- pair production with CLAS12 at* 11 GeV, `https://www.jlab.org/exp_prog/proposals/12/PR12-12-001.pdf`.

25. B. Pire, L. Szymanowski, J. Wagner, Phys. Rev. D **83**, 034009 (2011).
26. D. Mueller, B. Pire, L. Szymanowski, J. Wagner, Phys. Rev. D **86**, 031502 (2012).
27. H. Moutarde, B. Pire, F. Sabatie, L. Szymanowski, J. Wagner, Phys. Rev. D **87**, 054029 (2013).
28. CLAS Collaboration (E. Pasyuk), Chin. Phys. C **33**, 1205 (2009).
29. V.M. Braun, A.N. Manashov, D. Mueller, B.M. Pirnay, Phys. Rev. D **89**, 074022 (2014).
30. B. Pire, L. Szymanowski, J. Wagner, Phys. Rev. D **79**, 014010 (2009).
31. A. Accardi, J.L. Albacete, M. Anselmino, N. Armesto, E.C. Aschenauer, A. Bacchetta, D. Boer, W. Brooks *et al.*, arXiv:1212.1701 [nucl-ex].